

# Computational Screening of 2D Heterostructures for Efficient Photocatalytic Water Splitting

Forough Shobeyrian, Maryam Soleimani, Fazel Shojaei, Ali Lashani Zand, and Mahdi Pourfath\*

Cite This: *ACS Appl. Energy Mater.* 2025, 8, 9748–9759

Read Online

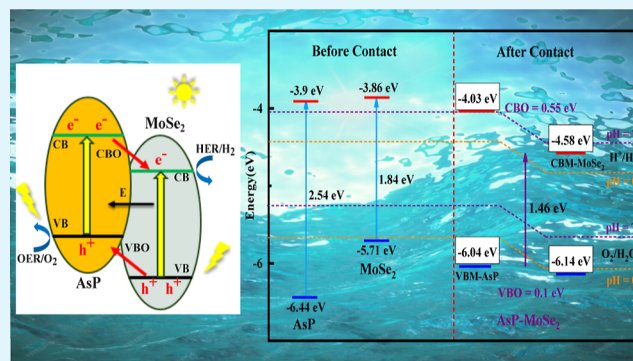
ACCESS |

Metrics &amp; More

Article Recommendations

**ABSTRACT:** In this study, 33 two-dimensional (2D) semi-conducting and nonmagnetic materials were screened to identify promising candidates for photocatalytic water splitting. Using density functional theory (DFT), the electronic properties of these materials were analyzed, and four type-II 2D heterostructures—AsP( $\beta$ )/MoSe<sub>2</sub>, GaSe/P( $\beta$ ), SiH/SnSe<sub>2</sub>, and Graphane/hC<sub>3</sub>B—were identified based on minimal lattice mismatch, atom count, and applied strain. The electronic and optical properties of these heterostructures were evaluated to assess their potential for photocatalytic water splitting. The results suggest that AsP( $\beta$ )/MoSe<sub>2</sub> is a promising candidate for efficient photocatalytic water splitting under visible light, with absorption coefficients comparable to those of high-performance perovskite solar cells.

**KEYWORDS:** 2D materials, heterostructures, hydrogen reduction reaction, photocatalytic water splitting, density functional theory



## 1. INTRODUCTION

Photocatalytic water splitting is a sustainable and promising solution to address the growing global energy demand while mitigating environmental challenges such as greenhouse gas emissions. This clean energy approach harnesses solar energy to generate hydrogen and oxygen through the splitting of water molecules, offering a carbon-free pathway toward energy independence.<sup>1,2</sup> Achieving efficient photocatalytic water splitting, however, requires advanced photocatalysts capable of absorbing visible light, ensuring robust stability, and facilitating effective charge separation and surface reactions. Ideal photocatalysts require a bandgap between 2 and 3 eV to absorb visible light, as well as suitable band edge positions to drive both the hydrogen evolution reaction (HER) and the oxygen evolution reaction (OER) without external reagents.<sup>3</sup> Current photocatalysts for water splitting, such as TiO<sub>2</sub>,<sup>4</sup> ZnO,<sup>5</sup> WO<sub>3</sub>,<sup>6</sup> CdS,<sup>7</sup> and ZnS,<sup>8</sup> have inherent limitations that hinder their efficiency, including wide bandgaps and high electron–hole recombination rates. These issues arise because electron–hole pairs are typically generated within the same region of the material, leading to rapid recombination and low quantum efficiency. To address this issue, heterojunctions—interfaces formed between two semiconductors with different bandgaps and distinct valence and conduction band positions—have been proposed as a promising solution.<sup>9,10</sup> Photocatalytic efficiency is improved by spatially separating the generated electrons and holes across the junction, thereby minimizing recombination. However, selecting the right components to form the heterojunction and

ensuring the formation of a clean interface that facilitates efficient charge migration are critical to achieving optimal performance.<sup>10,11</sup>

Two-dimensional (2D) nanosheets and layered materials have been recognized as highly promising candidates in areas such as photocatalysis,<sup>12</sup> energy storage,<sup>13</sup> electrocatalysis,<sup>14,15</sup> and organic catalysis.<sup>16</sup> Their monolayer structures, characterized by a large surface area-to-volume ratio and unique electronic properties, are particularly advantageous for photocatalysis. Compared to bulk materials, tunable bandgaps, enhanced light absorption, shorter charge migration paths, and improved charge separation are offered by 2D materials, contributing to superior catalytic performance. Despite these benefits, practical implementation of 2D materials remains challenging. One of the major hurdles is their wide bandgap, which limits light absorption to shorter wavelengths and reduces their ability to efficiently harness solar energy for redox reactions.<sup>17</sup>

A promising strategy to overcome these challenges involves the formation of van der Waals heterostructures (vdWHs), in which two or more 2D materials with complementary properties

Received: May 6, 2025

Revised: June 2, 2025

Accepted: June 9, 2025

Published: June 16, 2025



Table 1. Calculated Structural and Electronic Properties of 2D Materials with Respect to the Vacuum Level

material	lattice constant (Å)	$E_g$ (PBE) (eV)	$E_g$ (HSE06) (eV)	CBM (HSE06) (eV)	VBM (HSE06) (eV)	KPOINTS (CBM-VBM)	$\Delta H_f$ (eV/atom)	$E_{\text{Hull}}$ (eV/atom)
Graphane	$a = b = 2.53^a$	3.45	4.42	-0.98	-5.41	( $\Gamma - \Gamma$ )	-0.130	0.004
F-Graphane	$a = b = 2.60^b$	3.09	4.88	-4.24	-9.13	( $\Gamma - \Gamma$ )	-0.160	0.002
Sillican	$a = b = 3.88^c$	2.18	2.95	-2.65	-5.61	(M - $\Gamma$ )	0.005	0.005
F-Sillican	$a = b = 3.93^c$	0.65	1.57	-5.64	-7.22	( $\Gamma - \Gamma$ )	0.003	0.0025
Germanane	$a = b = 4.08^{cd}$	0.97	1.67	-3.69	-5.36	( $\Gamma - \Gamma$ )	0.079	0.079
F-Germanane	$a = b = 4.31^e$	0.01	0.28	-7.62	-7.91	( $\Gamma - \Gamma$ )	0.040	0.029
hBN	$a = b = 2.51^f$	4.65	5.73	-0.86	-6.60	( $\Gamma - K$ )	-1.282	0.00
hBP	$a = b = 3.20^g$	0.89	1.35	-4.08	-5.44	(K - K)	-0.90	0.02
hC <sub>3</sub> N	$a = b = 4.86^f$	0.39	1.05	-2.51	-3.57	( $\Gamma - M$ )	-1.0	0.00
hC <sub>3</sub> B	$a = b = 5.17^f$	0.64	1.83	-4.67	-6.51	(M - $\Gamma$ )	-0.85	0.00
$\alpha$ -P	$a = 3.30,$ $b = 4.59^g$	0.02	1.56	-3.91	-5.47	( $\Gamma - \Gamma$ )	0.038	0.038
$\beta$ -P	$a = b = 3.27^h$	1.94	2.81	-3.97	-6.78	(( $\Gamma - M$ ) $\rightarrow$ $\Gamma$ )	0.039	0.039
$\beta$ -As	$a = b = 3.61^h$	0.85	2.25	-3.58	-5.83	(( $\Gamma - M$ ) $\rightarrow$ K)	0.005	0.005
$\beta$ -AsP	$a = b = 3.45^i$	1.83	2.54	-3.90	-6.44	(( $\Gamma - M$ ) $\rightarrow$ $\Gamma$ )	0.017	0.017
SnS <sub>2</sub>	$a = b = 3.67^j$	1.56	2.36	-5.04	-7.40	(( $\Gamma - M$ ) $\rightarrow$ M)	-0.411	0.00
SnSe <sub>2</sub>	$a = b = 3.84^j$	0.76	1.38	-5.16	-6.55	(M $\rightarrow$ ( $\Gamma - M$ ))	-0.393	0.00
SnS	$a = 4.03,$ $b = 4.44^k$	1.23	2.31	-2.91	-5.22	(( $\Gamma - X$ ) $\rightarrow$ ( $\Gamma - Y$ ))	-0.407	0.041
SnSe	$a = 4.25,$ $b = 4.51^k$	0.89	1.61	-3.17	-4.79	(( $\Gamma - X$ ) $\rightarrow$ ( $\Gamma - Y$ ))	-0.389	0.039
GeS	$a = 3.63,$ $b = 4.54^k$	1.77	2.51	-3.11	-5.62	(( $\Gamma - X$ ) $\rightarrow$ $\Gamma$ )	-0.236	0.031
GeSe	$a = 3.97,$ $b = 4.27^k$	1.15	1.59	-3.23	-4.83	(( $\Gamma - Y$ ) $\rightarrow$ ( $\Gamma - Y$ ))	-0.205	0.025
MoS <sub>2</sub>	$a = b = 3.18^{jl}$	1.67	2.14	-4.23	-6.37	(K - K)	-0.901	0.00
MoSe <sub>2</sub>	$a = b = 3.32^{jl}$	1.43	1.84	-3.86	-5.71	(K - K)	-0.720	0.00
MoTe <sub>2</sub>	$a = b = 3.55^{jl}$	1.07	1.49	-3.70	-5.21	(K - K)	-0.305	0.00
WS <sub>2</sub>	$a = b = 3.18^{jl}$	1.69	2.36	-3.73	-6.10	(K - K)	-0.869	0.00
WSe <sub>2</sub>	$a = b = 3.32^{jl}$	1.40	2.08	-3.39	-5.48	(K - K)	-0.620	0.00
WTe <sub>2</sub>	$a = b = 3.51^{jl}$	1.10	1.59	-3.36	-4.95	(K - K)	-0.112	0.010
GaS	$a = b = 3.58^{mn}$	2.60	3.38	-3.56	-6.94	(M $\rightarrow$ ( $\Gamma - M$ ))	-0.663	0.00
GaSe	$a = b = 3.75^{mn}$	2.20	3.12	-3.35	-6.47	( $\Gamma \rightarrow$ ( $\Gamma - M$ ))	-0.621	0.00
GaTe	$a = b = 4.12^{mn}$	1.46	2.13	-3.65	-5.78	(M $\rightarrow$ ( $\Gamma - M$ ))	-0.361	0.002
InS	$a = b = 3.91^{mn}$	1.76	2.61	-4.39	-7	( $\Gamma \rightarrow$ ( $\Gamma - M$ ))	-0.544	0.00
InSe	$a = b = 4.06^{mn}$	1.50	2.26	-4.28	-6.55	( $\Gamma \rightarrow$ ( $\Gamma - M$ ))	-0.519	0.00
InTe	$a = b = 4.37^{mn}$	1.39	2.02	-3.88	-5.90	( $\Gamma \rightarrow$ ( $\Gamma - M$ ))	-0.311	0.00
BeO	$a = b = 2.67^o$	5.32	6.80	-1.09	-7.89	( $\Gamma - K$ )	-2.11	0.00

<sup>a</sup>Ref 43. <sup>b</sup>Ref 44. <sup>c</sup>Ref 45. <sup>d</sup>Ref 46. <sup>e</sup>Ref 47. <sup>f</sup>Ref 48. <sup>g</sup>Ref 49. <sup>h</sup>Ref 50. <sup>i</sup>Ref 51. <sup>j</sup>Ref 52. <sup>k</sup>Ref 53. <sup>l</sup>Ref 54. <sup>m</sup>Ref 55. <sup>n</sup>Ref 56. <sup>o</sup>Ref 57.

are stacked to create heterojunctions. These heterostructures facilitate tunable band alignments, high carrier mobility, and enhanced light absorption, enabling precise control over their electronic and optical properties for diverse applications.<sup>18</sup> Extensive research has explored various 2D heterostructures, including In<sub>2</sub>Se<sub>3</sub>/SnP,<sup>19</sup> PtS<sub>2</sub>/As,<sup>20</sup> MoS<sub>2</sub>-CrXY (X  $\neq$  Y; S, Se, Te),<sup>21</sup> GaTe/SnS<sub>2</sub>,<sup>22</sup> GeSe/SnSe,<sup>23</sup> GeC/MXY (M = Zr, Hf; X, Y = S, Se),<sup>24</sup> C<sub>2</sub>N/BlueP,<sup>25</sup> SiH/g-C<sub>3</sub>N<sub>4</sub>,<sup>26</sup> ZnO/BSe,<sup>27</sup> BlueP/BSe,<sup>28</sup> g-C<sub>3</sub>N<sub>4</sub>/InSe,<sup>29</sup> and BlackP/Bismuth.<sup>30</sup> A notable example is the Janus-MoSSe/WSe<sub>2</sub> system, where asymmetric atomic arrangements generate dipole fields that significantly improve carrier dynamics, demonstrating the potential for enhancing photocatalytic performance.<sup>31</sup> Among various heterostructure types, type-II vdWHs are especially attractive due to their spatial separation of charge carriers. In these systems, electrons and holes are confined to different layers via staggered band alignment, reducing recombination rates and enhancing charge transfer. For example, CdX/C<sub>2</sub>N heterostructures exhibit efficient spatial carrier separation and have demonstrated photocatalytic hydrogen production even in challenging environments such as seawater.<sup>32</sup>

In contrast, Z-scheme charge transfer mechanisms mimic natural photosynthesis by promoting indirect charge transfer. Rather than complete spatial separation, Z-scheme heterostructures retain electrons in the conduction band of one material and holes in the valence band of the other, enabling high redox potentials. This mechanism is particularly advantageous for photocatalytic reactions requiring high overpotentials, such as HER and OER. The SnS<sub>2</sub>/ $\beta$ -As heterostructure is an example where the Z-scheme enhances charge utilization while maintaining strong photocatalytic performance under solar irradiation.<sup>33</sup> These advancements underscore the importance of interface engineering and heterostructure design.<sup>34,35</sup> Additionally, computational methods such as density functional theory (DFT), often combined with machine learning, have enabled high-throughput screening and design of novel heterostructures, as illustrated in recent databases of Janus III-VI systems for solar applications.<sup>36</sup>

In this work, a computational screening of 33 semiconducting and nonmagnetic 2D materials was performed using DFT to investigate their electronic properties. Based on criteria including lattice mismatch, atom count, and strain, four

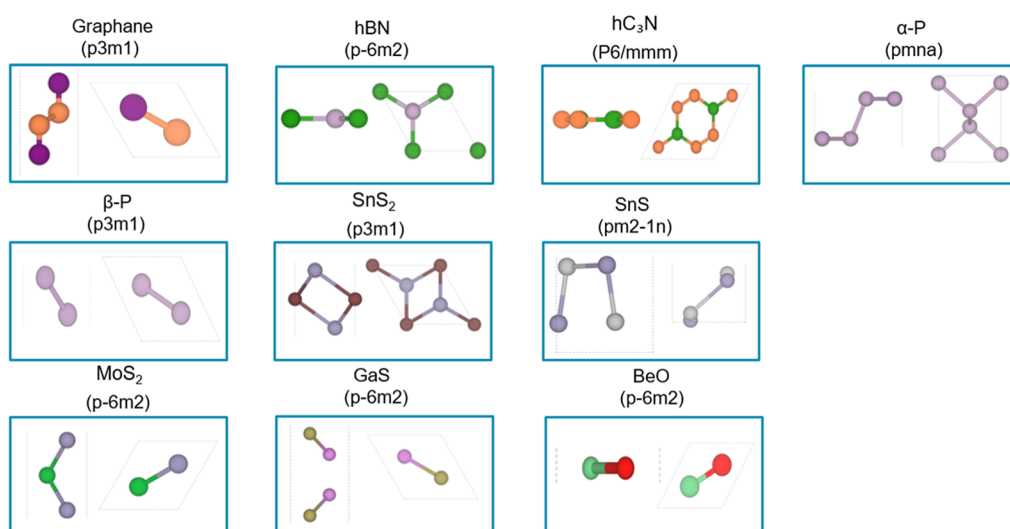


**Figure 1.** Top and side views of representative materials from the 10 categories, along with their corresponding space groups.

heterostructures—AsP( $\beta$ )/MoSe<sub>2</sub>, GaSe/P( $\beta$ ), SiH/SnSe<sub>2</sub>, and Graphane/hC<sub>3</sub>B—were selected for further analysis. Their electronic and optical properties were examined to assess their suitability for photocatalytic water splitting. Among them, AsP( $\beta$ )/MoSe<sub>2</sub> demonstrated particularly favorable optical absorption characteristics under visible light, identifying it as a strong candidate for efficient water splitting.

## 2. METHODS AND COMPUTATIONAL DETAILS

Density functional theory calculations were performed using the Vienna Ab initio Simulation Package (VASP).<sup>37</sup> The Perdew–Burke–Ernzerhof (PBE) functional within the generalized gradient approximation (GGA) was used to calculate the exchange–correlation energy. The projector augmented-wave (PAW) method was used to describe the interaction between valence electrons and ions. As PBE underestimates semiconductor bandgaps, the Heyd–Scuseria–Ernzerhof hybrid functional (HSE06)<sup>38</sup> was employed to accurately evaluate electronic and optical properties. van der Waals (vdW) interactions were included using the DFT-D3 correction.<sup>39</sup>

Atomic positions were optimized using a conjugate gradient algorithm until the force on each atom was smaller than 0.001 eV/Å. The Brillouin zone was sampled using an 8 × 8 × 1 Monkhorst–Pack *k*-point mesh. A vacuum spacing of 25 Å was applied along the *z*-direction to avoid interactions between periodic images. To account for polarization effects in asymmetric systems, a dipole correction was applied. The dipole moment was calculated by integrating the charge density over the unit cell. This approach allows quantifying net polarization by capturing the spatial distribution of charge.<sup>40</sup>

Optical absorption spectra were estimated by incorporating excitonic effects using the Tamm–Dancoff approximation (TDA) and the Casida equation.<sup>41</sup> The absorption coefficient  $\alpha(\omega)$  was calculated using

$$\alpha(\omega) = \sqrt{2}\omega \sqrt{\frac{\epsilon_1^2 + \epsilon_2^2 - \epsilon_1}{2}} \quad (1)$$

where  $\epsilon_1$  and  $\epsilon_2$  are the real and imaginary parts of the dielectric function, respectively.

## 3. RESULTS AND DISCUSSION

### 3.1. Computational Screening and Material Selection.

A computational screening was conducted on 33 two-dimensional (2D) materials, primarily sourced from the Materials Project and the Computational 2D Materials Database (C2DB),<sup>42</sup> with a focus on nonmagnetic semiconducting

materials. Additionally, some structures were derived via atomic substitution using known 2D templates based on prior studies, rather than being novel to this work. All structures were fully optimized to ensure stability, and only the most stable phase—defined by the lowest total energy—was considered for further analysis.

For each structure, the enthalpy of formation and energy above the convex hull were computed using the bulk energy of each constituent element to assess thermodynamic stability and synthesizability (see Table 1). The results confirm that the proposed structures are thermodynamically stable with respect to their elemental constituents. Furthermore, the low energy above the convex hull values suggest that these structures are close to known stable phases and are likely to be experimentally realizable.

Band structures of the 2D semiconductors were aligned based on the vacuum level, leading to the identification of ten type-II heterostructures. This alignment methodology enabled the screening of promising 2D materials for electronic and optoelectronic applications. The materials surveyed include transition metal dichalcogenides (TMDs), Group-III and IV metal monochalcogenides, and hydrogenated or fluorinated derivatives of elemental 2D materials such as graphane, germanane, and silicane. Also included were hexagonal boron nitride, phosphorene, and arsenene.

These materials were categorized into ten groups according to their atomic arrangements and space groups. Representative top and side views for each category, along with the number of structures per group, are shown in Figure 1. The MX<sub>2</sub> structure (space group *P-6m2*) is the most prevalent among the identified semiconductors. The lattice constants of all optimized structures are in good agreement with previously reported values (see Table 1).<sup>43–57</sup>

A systematic trend was observed in the lattice parameters: for materials sharing the same cation, the lattice constant increases with the atomic number of the anion, reflecting the larger ionic radius and weaker cation–anion interaction. Table 1 also includes electronic bandgaps, along with conduction band minimum (CBM) and valence band maximum (VBM) positions. A comparison between bandgaps calculated using the PBE and HSE06 functionals reveals that the HSE06 method

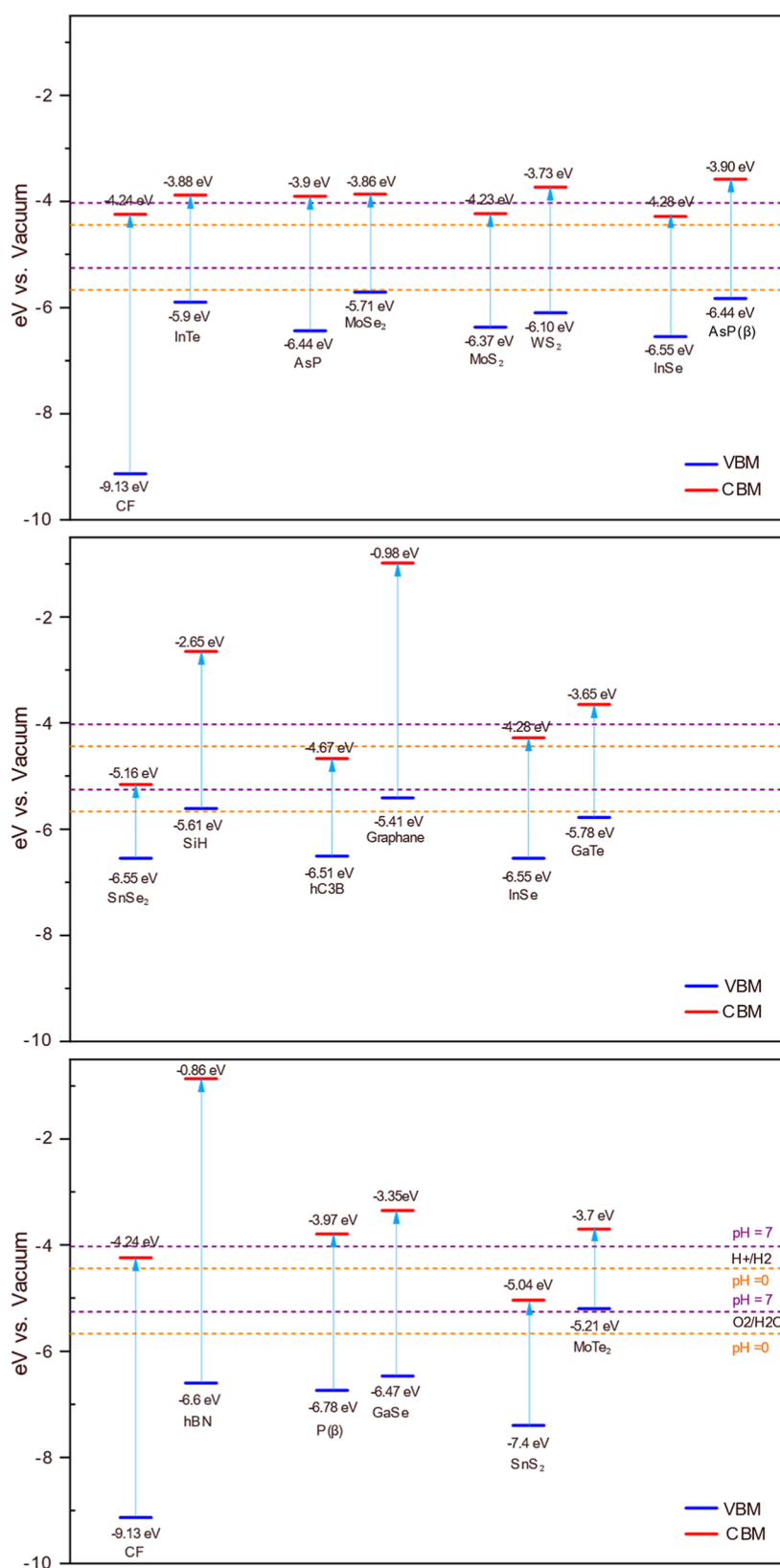


**Figure 2.** Positions of the VBM and CBM calculated using the HSE06 functional for the studied 2D materials. The oxidation and reduction potentials of water at pH = 0 (dashed orange lines) and pH = 7 (dashed purple lines) are also shown.

significantly improves the accuracy, yielding values that closely match experimental data.<sup>39</sup>

**3.2. Selection and Screening of Type-II Heterostructures.** Heterostructures play a pivotal role in modern electronic

and optoelectronic devices, as band alignment between different materials governs charge transport characteristics and overall device performance. Semiconductor heterostructures are typically classified into three band alignment types: type I

Table 2. Calculated Lattice Constants, Number of Atoms, Strain, and Electronic Properties for the Constructed Heterostructures

heterostructure	lattice constant first layer (Å)	lattice constant second Layer (Å)	lattice constant (heterostructure) (Å)	number of atoms	strain	$E_{\text{binding}}$ (eV/Å <sup>2</sup> )	$E_{\text{g}}$ (HSE06) (eV)
AsP( $\beta$ )/MoSe <sub>2</sub>	3.45(3.47) <sup>a</sup>	3.32(3.33) <sup>b</sup>	3.32	5	1.76	18.25	1.46
GaSe/P( $\beta$ )	3.75(3.75) <sup>c</sup>	3.27(3.32) <sup>d</sup>	6.49	20	0.36	10.12	2.28
SiH/SnSe <sub>2</sub>	3.88(3.88) <sup>e</sup>	3.84(3.82) <sup>f</sup>	3.88	7	0.51	12.70	0.44
hC <sub>3</sub> B/graphane	5.17(5.17) <sup>g</sup>	2.53(2.54) <sup>h</sup>	5.07	24	0.88	8.10	0.64

<sup>a</sup>Ref 51. <sup>b</sup>Ref 54. <sup>c</sup>Ref 63. <sup>d</sup>Ref 50. <sup>e</sup>Ref 46. <sup>f</sup>Ref 52. <sup>g</sup>Ref 63. <sup>h</sup>Ref 43.

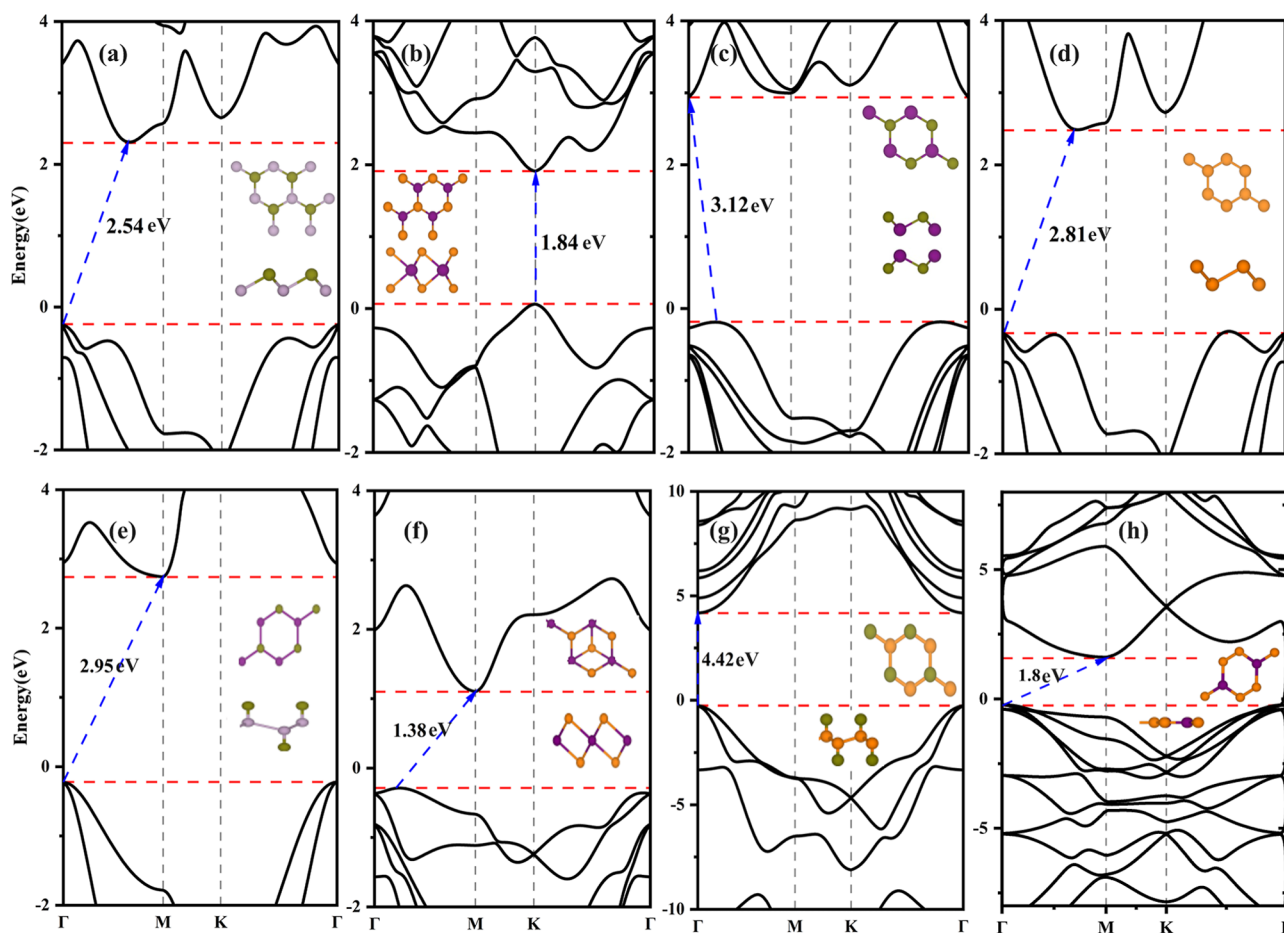


**Figure 3.** Geometrical and electronic band structures of (a) AsP (green and purple spheres for As and P atoms, respectively), (b) MoSe<sub>2</sub> (orange and purple spheres for Se and Mo atoms, respectively), (c) GaSe (green and purple spheres for Ga and Se atoms, respectively), (d) P (orange spheres for P atoms), (e) SiH (green and purple spheres for H and Si atoms, respectively), (f) SnSe<sub>2</sub> (orange and purple spheres for Se and Sn atoms, respectively), (g) Graphane (orange and green spheres for C and H atoms, respectively), and (h) hC<sub>3</sub>B (orange and purple spheres for C and B atoms, respectively) monolayers.

(straddling gap), type II (staggered gap), and type III (broken gap).<sup>58</sup> Among these, type II heterostructures are especially promising for optoelectronic and photocatalytic applications due to their ability to spatially separate photoexcited electron–hole pairs.<sup>59,60</sup> This separation is facilitated by the staggered alignment of the conduction and valence bands, akin to a semiconductor p–n junction, and has been widely employed in photovoltaic and rectifying devices. Motivated by these advantages, we focused on identifying and analyzing type-II heterostructures among 2D semiconductors. By comparing the band gaps and band edge positions of the 33 screened 2D materials summarized in Table 1, ten combinations were identified that form type-II heterojunctions. The positions of the VBM and CBM were calculated using the HSE06 hybrid functional and are illustrated in Figure 2.

To construct the heterostructures, we used the CellMatch algorithm to search for commensurate supercells with minimal lattice mismatch and reduced computational cost.<sup>61</sup> Only combinations with fewer than 24 atoms per unit cell and strain below 3% were retained. Based on this evaluation, the heterostructures AsP( $\beta$ )/MoSe<sub>2</sub>, GaSe/P( $\beta$ ), SiH/SnSe<sub>2</sub>, and hC<sub>3</sub>B/Graphane were selected. The structural and electronic properties of the final candidates, including optimal lattice parameters, binding energy, and electronic bandgaps, are provided in Table 2.

To further refine the analysis, we calculated the binding energy per unit area using the relation:  $E_{\text{binding}} = (E_{\text{A}} + E_{\text{B}} - E_{\text{AB}})/S$ , where  $E_{\text{AB}}$  is the total energy of the heterostructure,  $E_{\text{A}}$  and  $E_{\text{B}}$  are the energies of the isolated monolayers, and  $S$  is the interfacial area. The resulting values for the selected systems—

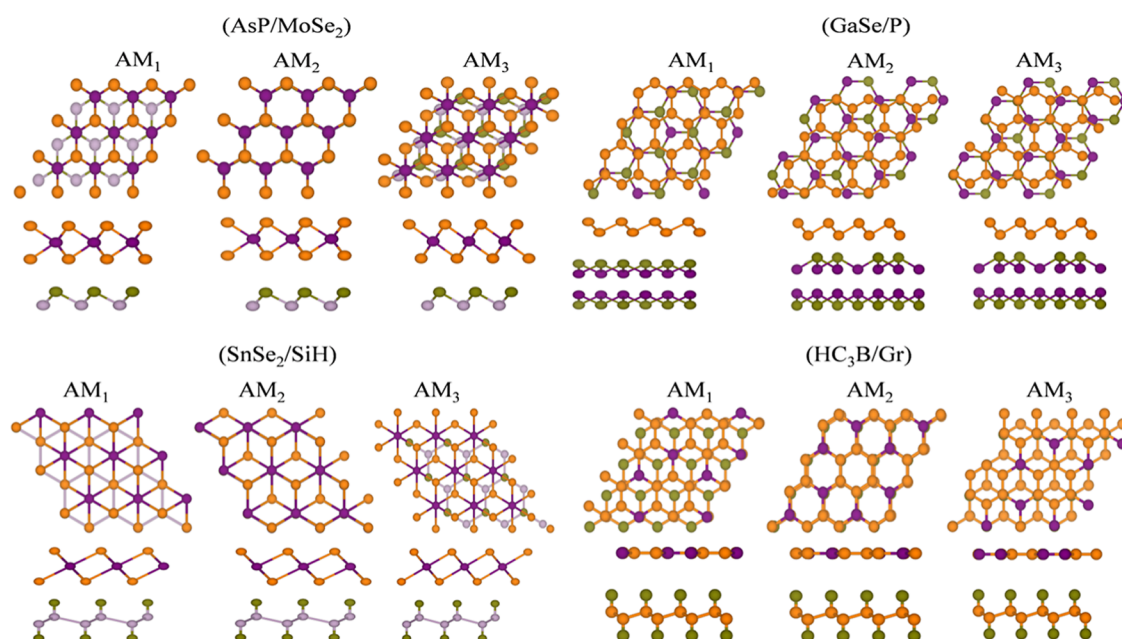


**Figure 4.** Top view (upper panel) and side view (lower panel) of the heterostructures in different possible stacking configurations: AM<sub>1</sub>, AM<sub>2</sub>, and AM<sub>3</sub>.

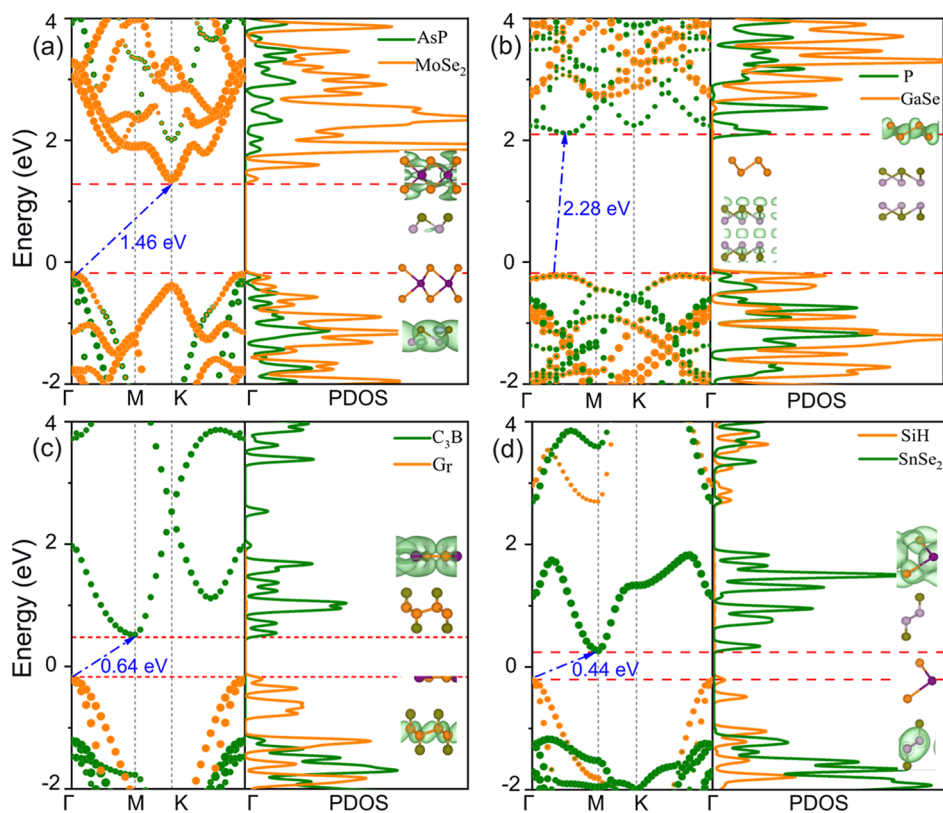


**Figure 5.** Band structures and projected density of states (PDOS) for (a) AsP( $\beta$ )/MoSe<sub>2</sub>, (b) GaSe/P( $\beta$ ), (c) hC<sub>3</sub>B/Graphane, and (d) SiH/SnSe<sub>2</sub>. The charge density distributions of the CBM and VBM are shown as insets within the PDOS plots. The Fermi energy level in the HSE06 calculations is set to 0 eV.

AsP( $\beta$ )/MoSe<sub>2</sub> (18.25 eV/Å<sup>2</sup>), GaSe/P( $\beta$ ) (10.12 eV/Å<sup>2</sup>), SiH/SnSe<sub>2</sub> (12.70 eV/Å<sup>2</sup>), and hC<sub>3</sub>B/Graphane (8.10 eV/Å<sup>2</sup>)—are consistently lower than their homobilayer counterparts, indicating weaker interlayer interactions but favorable energetic stability.<sup>64</sup> The hexagonal monolayer geometries and their band structures are shown in Figure 3. All systems exhibit

semiconducting behavior, with MoSe<sub>2</sub> and Graphane showing direct gaps and others exhibiting indirect bandgaps. The computed lattice constants and bandgaps are in close agreement with experimental and theoretical benchmarks.<sup>43,46,50–52,54,62,63</sup>

According to Figure 4, the studied heterostructures exhibit three distinct stacking configurations, which are called AM<sub>1</sub>,

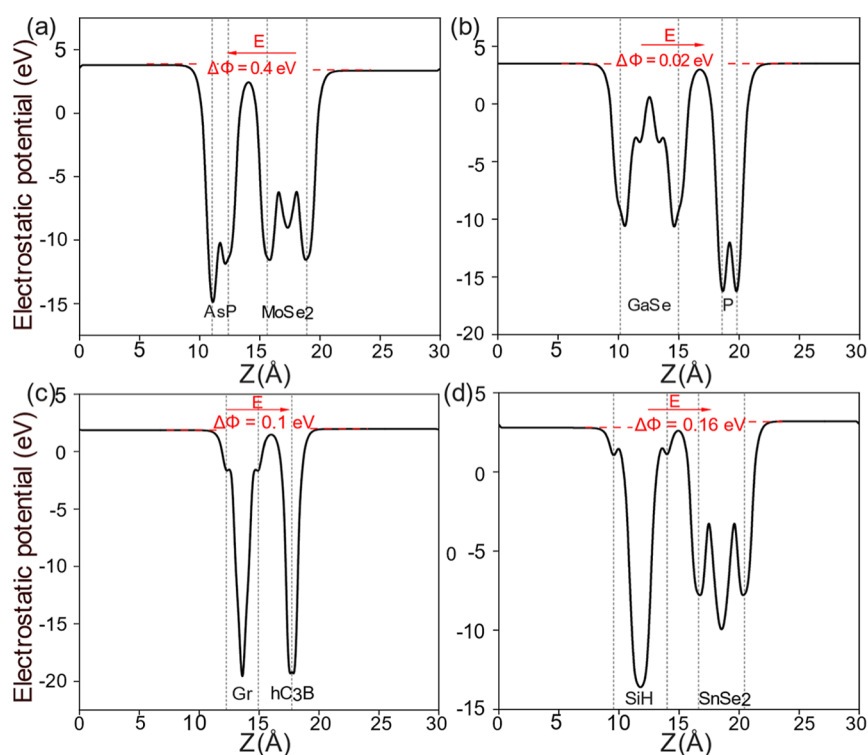


**Figure 6.** Electrostatic potential and vacuum level difference ( $\Delta\Phi$ ) between the two surfaces in (a) AsP( $\beta$ )/MoSe<sub>2</sub>, (b) GaSe/P( $\beta$ ), (c) hC<sub>3</sub>B/Graphane, and (d) SiH/SnSe<sub>2</sub> heterostructures. Light gray lines indicate the positions of the monolayers.

**Table 3. Structural and Electronic Parameters of the Heterostructures, Including Dipole Moment, Surface Area, Thickness, Internal Electric Field, and Charge Transfer**

heterostructure	dipole moment (eÅ)	surface area (Å <sup>2</sup> )	thickness (Å)	electric field (V/m)	charge transfer (e)
AsP( $\beta$ )/MoSe <sub>2</sub>	0.022	9.545	4.631	$9.11 \times 10^8$	0.014 (donor/acceptor)
GaSe/P( $\beta$ )	0.016	36.533	8.515	$2.39 \times 10^7$	0.008 (acceptor/donor)
SiH/SnSe <sub>2</sub>	0.029	13.054	9.100	$1.72 \times 10^8$	0.007 (acceptor/donor)
hC <sub>3</sub> B/graphane	0.081	22.305	5.453	$3.23 \times 10^8$	0.015 (acceptor/donor)

AM<sub>2</sub>, and AM<sub>3</sub>, respectively. After calculating the total energy of these compositions, the lowest total energy was found for the AM<sub>1</sub> structure, indicating van der Waals-type interaction. The interlayer height ( $H_i$ ) in the AsP( $\beta$ )/MoSe<sub>2</sub>, GaSe/P( $\beta$ ), hC<sub>3</sub>B/Graphane, and SiH/SnSe<sub>2</sub> heterostructures with the AM<sub>1</sub> composition is 3.27, 3.65, 2.20, and 2.77 Å, respectively. Further research has also been conducted based on the AM<sub>1</sub> composition.

The HSE06 band structure results in Figure 5 confirm that the studied heterostructures are semiconductors with indirect band gaps: AsP( $\beta$ )/MoSe<sub>2</sub> (1.46 eV), GaSe/P( $\beta$ ) (2.28 eV), hC<sub>3</sub>B/Graphane (0.64 eV), and SiH/SnSe<sub>2</sub> (0.44 eV). In AsP( $\beta$ )/MoSe<sub>2</sub>, the CBM is located at the  $K$  point, while the VBM appears at  $\Gamma$ . For GaSe/P( $\beta$ ), both the VBM and CBM are located between the  $\Gamma$  and  $M$  points. In the remaining two heterostructures, the VBM is at  $\Gamma$ , and the CBM is at  $M$ . The PDOS and charge density distributions reveal that the VBM is primarily contributed by one layer (AsP( $\beta$ ), GaSe, Graphane, and SiH), while the CBM is dominated by the other (MoSe<sub>2</sub>, P( $\beta$ ), hC<sub>3</sub>B, and SnSe<sub>2</sub>), confirming charge separation in these heterostructures. The operation of a Type II heterojunction can either follow a standard mechanism, where charge carriers move thermodynamically across the interface, or a Z-scheme, where electrons and holes recombine kinetically at the interface between the two semiconductors.<sup>65</sup> Experimental techniques

such as photoluminescence spectroscopy, electrochemical impedance spectroscopy, and X-ray photoelectron spectroscopy offer a comprehensive understanding of charge transfer mechanisms and can aid in distinguishing between standard Type II and Z-scheme heterojunctions.<sup>66</sup> However, differentiating between these two types of heterojunctions based solely on theoretical calculations remains challenging.

In this work, after examining the alignment of energy bands, built-in electric fields have been used to track the direction of charge transfer, which allows for an initial assumption regarding the heterojunction mechanism. This preliminary guess serves as a predictor for determining whether the system follows the standard Type II model or the Z-scheme model. To characterize the built-in electric field in the studied heterostructures the averaged electrostatic potentials along the stacking direction are plotted in Figure 6, represented by red curves. The electrostatic potential difference between the monolayers forming the heterostructures AsP( $\beta$ )/MoSe<sub>2</sub>, GaSe/P( $\beta$ ), hC<sub>3</sub>B/Graphane, and SiH/SnSe<sub>2</sub> is found to be 0.4, 0.02, 0.1, and 0.16 eV, respectively, indicating the formation of internal electric field. The direction of the built-in electric field points from one monolayer to another, labeled with a red arrow in Figure 6.

It is worth mentioning that if the built-in electric field is a consequence of surface charge polarization, either electrons (in the positive layer) or holes (in the negative layer) transfer from

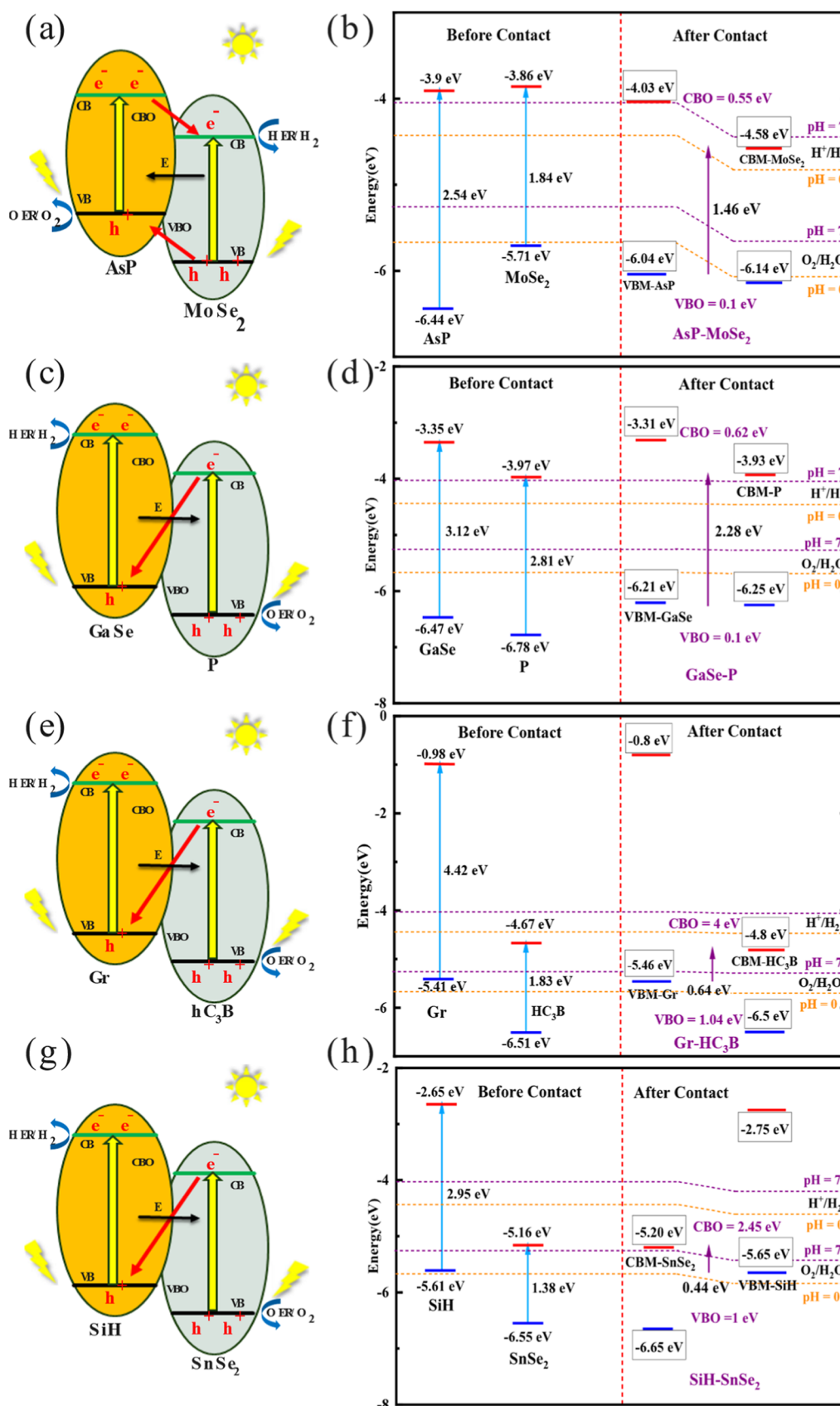


**Figure 7.** Photogenerated charge migration path and the band alignment of the (a,b) AsP( $\beta$ )/MoSe<sub>2</sub>, (c,d) GaSe/P( $\beta$ ), (e,f) hC<sub>3</sub>B/Graphane, and (g,h) SiH/SnSe<sub>2</sub> vdW heterostructures.

one layer to the other, which modifies the electronic structures in order to screen the charge polarization.<sup>67</sup> This can be

observed in AsP( $\beta$ )/MoSe<sub>2</sub>, GaSe/P( $\beta$ ), and SiH/SnSe<sub>2</sub>, where charge transfer (Bader analysis)<sup>68</sup> occurs to reduce the polarized

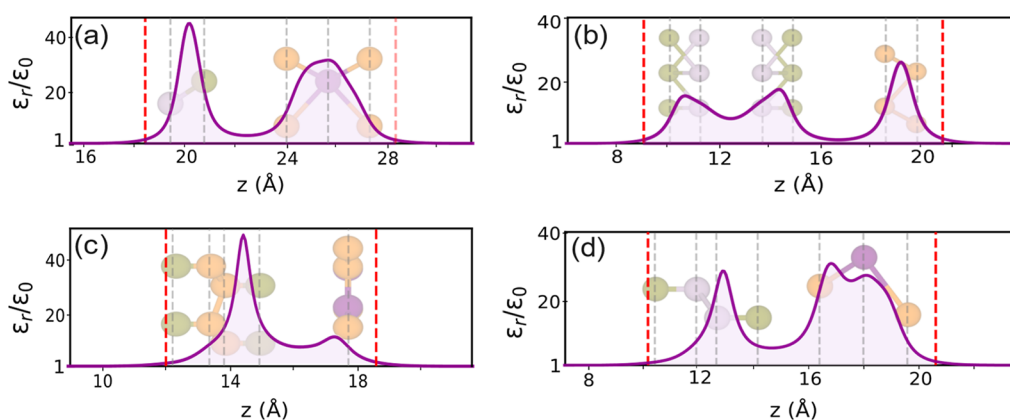


**Figure 8.** Out-of-plane high-frequency dielectric constant profiles for the vdW heterostructures: (a) AsP( $\beta$ )/MoSe<sub>2</sub>, (b) GaSe/P( $\beta$ ), (c) hC<sub>3</sub>B/Graphane, and (d) SiH/SnSe<sub>2</sub>.

built-in electric field (Table 3). However, in the case of hC<sub>3</sub>B/Graphane, electrons move from Graphane to hC<sub>3</sub>B, creating an imbalance in charge density at the interface, which leads to the formation of a built-in electric field. This built-in electric field, which is not due to polarization, should be coupled with an external electric field to induce polarization and transfer of electrons from C<sub>3</sub>B to Graphane. Following the previous study,<sup>69</sup> the strength of this built-in electric field can be estimated by  $E = P/\epsilon Sd$  where  $P$  is the intrinsic dipole moment,  $\epsilon$  is the dielectric constant,  $S$  is the surface area, and  $d$  is the thickness of the heterostructure. The calculated dipole moments are reported in Table 3.

The type-II band structure of the AsP( $\beta$ )/MoSe<sub>2</sub> vdW heterostructure provides the ability to separate photogenerated electrons and holes, making it suitable as a photocatalyst for water splitting. As shown in Figure 7a, the AsP( $\beta$ )/MoSe<sub>2</sub> vdW heterostructure absorbs photon energy larger than the bandgap of the MoSe<sub>2</sub> and AsP( $\beta$ ) layers. The photogenerated electrons are excited in the conduction band (CB) of the AsP( $\beta$ ) and MoSe<sub>2</sub> layers, while the photogenerated holes remain in the valence band (VB). The photogenerated electrons in the CB of the AsP( $\beta$ ) layer then move to the CB of the MoSe<sub>2</sub> layer due to the CB offset (CBO), as shown in Figure 7a. Similarly, the photogenerated holes in the MoSe<sub>2</sub> layer transfer to the VB of the AsP( $\beta$ ) layer due to the VB offset (VBO). Therefore, the photogenerated electrons are continuously promoted from the CB of the AsP( $\beta$ ) layer to the MoSe<sub>2</sub> layer, while the photogenerated holes keep moving from the VB of the MoSe<sub>2</sub> layer to the AsP( $\beta$ ) layer under continuous solar photodynamic conditions, inducing a circulating flow of photogenerated electrons and holes (Wang et al., 2018b). Furthermore, the band edge positions of the AsP( $\beta$ )/MoSe<sub>2</sub> vdW heterostructure are also calculated in Figure 7b to investigate the photocatalytic driving potential for water splitting. At pH 0 and 7, the standard potential energies of the hydrogen evolution reaction (HER) and the oxygen evolution reaction (OER) are  $-4.42$  and  $-4.02$  eV, and  $-5.67$  and  $-5.25$  eV, respectively (Wang et al., 2018a).

The obtained band alignment of the monolayered MoSe<sub>2</sub>, AsP( $\beta$ ), and the AsP( $\beta$ )/MoSe<sub>2</sub> vdW heterostructure is demonstrated in Figure 7b, which shows that the monolayers MoSe<sub>2</sub>, AsP( $\beta$ ), and the AsP( $\beta$ )/MoSe<sub>2</sub> vdW heterostructure have suitable band edge positions to induce the HER and OER at pH 0. Thus, the AsP( $\beta$ )/MoSe<sub>2</sub> vdW heterostructure can be considered a potential photocatalyst for water decomposition.

On the other hand, in the heterostructures GaSe/P( $\beta$ ), hC<sub>3</sub>B/Graphane, and SiH/SnSe<sub>2</sub>, the electrons in the VBM of both layers are excited to form electron–hole pairs when exposed to light. Due to the internal electric field, the charge carriers generated by light move in the structures, as shown in Figure 7c, e.g. Additionally, there is mutual repulsion between two CB electrons or between two VB holes, which causes the electrons of the CB in the monolayer P( $\beta$ ) or SnSe<sub>2</sub> to recombine with the VB holes of the GaSe or SiH monolayer.

According to the above analysis, the heterostructures hC<sub>3</sub>B/Graphane, GaSe/P( $\beta$ ), and SiH/SnSe<sub>2</sub> form a Z-scheme, which effectively enhances carrier separation and carrier lifetime generated by light. Figure 7d shows that the monolayers and the heterostructure GaSe/P( $\beta$ ) are well positioned to facilitate HER and OER at pH 0 and 7.

Therefore, the heterostructure GaSe/P( $\beta$ ) can be considered a potential photocatalyst for water splitting. From the band alignment shown in Figure 7f, the hC<sub>3</sub>B/Graphane heterostructure is not suitable for enabling HER and OER at both pH 0 and pH 7. As shown in Figure 7h, the heterostructure of SiH/SnSe<sub>2</sub> is suitably positioned for the generation of OER at pH 7.

One important factor influencing the effectiveness of charge separation and exciton dissociation in photocatalytic heterostructures is the dielectric constant.<sup>70</sup> The spatially resolved dielectric profile,  $\epsilon(z)$ , was computed using the PBE functional, following the method described in ref 70, in which an external electric field is applied along the out-of-plane direction (Figure 8). In this method, a simulation cell containing the heterostructure is constructed and embedded in vacuum to eliminate spurious interactions arising from periodic boundary conditions. To ensure electrostatic decoupling, a vacuum buffer of at least 20 Å is included along the out-of-plane axis. Based on this setup, the induced charge density, associated polarization, effective electric field, and the resulting dielectric profile are determined. Significant differences in dielectric response may be seen in the spatial distribution of  $\epsilon(z)$ , especially at the heterostructures where enhanced screening is caused by interfacial polarization and induced charge redistribution.

Strong and spatially extended dielectric screening that promotes effective exciton separation is demonstrated by the broad and rising dielectric peaks along the interface of the AsP/MoSe<sub>2</sub> and GaSe/P( $\beta$ ) systems. On the other hand, hC<sub>3</sub>B/Graphane exhibits a more localized dielectric response, indicating that polarization effects are contained within a smaller area. The complex interlayer interactions and potential

covalent bonding contributions are reflected in the SiH/SnSe<sub>2</sub> heterostructure's numerous distinct peaks in  $\epsilon(z)$ . These results emphasize the critical role dielectric engineering plays in designing 2D heterostructures for photocatalytic applications, where improved interfacial dielectric constants can greatly enhance overall performance and charge carrier separation.

As a photocatalyst for water splitting, the ability to absorb light also plays an important role. Finally, the optical absorption of the studied heterostructures was investigated. Figure 9 shows the

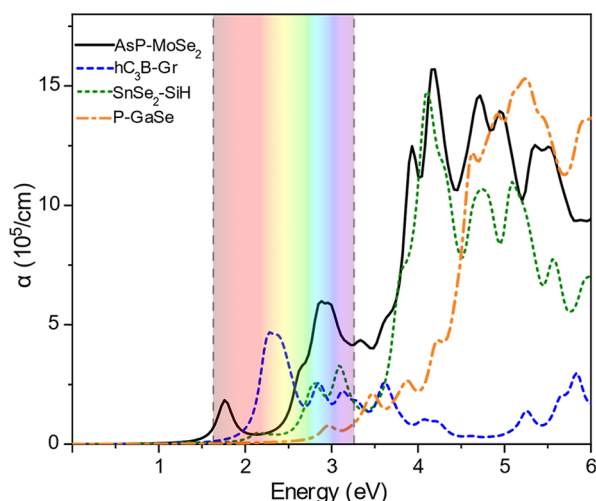


Figure 9. Calculated optical absorption spectra of the heterostructures.

absorption coefficients for light incident to the plane of the heterostructure. It can be seen that, except for the SiH/SnSe<sub>2</sub> and GaSe/P( $\beta$ ) structures, which have relatively small light absorption in the visible spectrum range, the other two structures, like the perovskite materials used in solar cells, have high absorption (about  $1.5 \times 10^5 \text{ cm}^{-1}$ ).

#### 4. CONCLUSIONS

In this study, we conducted a computational screening of 33 nonmagnetic semiconducting 2D materials to identify candidates for photocatalytic water splitting. Using DFT calculations, we identified four promising type-II 2D heterostructures—AsP( $\beta$ )/MoSe<sub>2</sub>, GaSe/P( $\beta$ ), SiH/SnSe<sub>2</sub>, and Graphane/hC<sub>3</sub>B—based on criteria such as low lattice mismatch and minimal strain.

Our analysis showed that AsP( $\beta$ )/MoSe<sub>2</sub> is highly promising for photocatalytic water splitting under visible light, with absorption coefficients comparable to efficient perovskite solar cells. GaSe/P( $\beta$ ) and SiH/SnSe<sub>2</sub> also demonstrated favorable properties, with GaSe/P( $\beta$ ) suitable for both hydrogen and oxygen evolution reactions at various pH levels, and SiH/SnSe<sub>2</sub> suitable for oxygen evolution at pH 7. The hC<sub>3</sub>B/Graphane heterostructure was less effective due to its band alignment. Overall, this study highlights the promise of 2D heterostructures for photocatalytic water splitting and sets the stage for future experimental validation and development in renewable energy applications.

#### AUTHOR INFORMATION

##### Corresponding Author

Mahdi Pourfath — School of Electrical and Computer Engineering, College of Engineering, University of Tehran, Tehran 14395-515, Iran; Institute for Microelectronics, A-

1040 Vienna, Austria; [orcid.org/0000-0002-8053-578X](https://orcid.org/0000-0002-8053-578X);

Email: [pourfath@ut.ac.ir](mailto:pourfath@ut.ac.ir), [pourfath@iue.tuwien.ac.at](mailto:pourfath@iue.tuwien.ac.at)

#### Authors

Forough Shobeyrian — School of Electrical and Computer Engineering, College of Engineering, University of Tehran, Tehran 14395-515, Iran

Maryam Soleimani — Department of Materials Science, University of Milano-Bicocca, 20125 Milano, Italy

Fazel Shojaei — Department of Chemistry, Faculty of Nano and Bioscience and Technology, Persian Gulf University, Bushehr 75169, Iran; [orcid.org/0000-0002-2496-7289](https://orcid.org/0000-0002-2496-7289)

Ali Lashani Zand — School of Electrical and Computer Engineering, College of Engineering, University of Tehran, Tehran 14395-515, Iran; [orcid.org/0000-0003-1711-5704](https://orcid.org/0000-0003-1711-5704)

Complete contact information is available at:

<https://pubs.acs.org/10.1021/acsaem.5c01342>

#### Notes

The authors declare no competing financial interest.

#### ACKNOWLEDGMENTS

The authors acknowledge TU Wien Bibliothek for financial support through its Open Access Funding Programme.

#### REFERENCES

- (1) Gan, X.; Lei, D.; Wong, K.-Y. Two-Dimensional Layered Nanomaterials for Visible-Light-Driven Photocatalytic Water Splitting. *Mater. Today Energy* **2018**, *10*, 352–367.
- (2) Haryanto, A.; Fernando, S.; Murali, N.; Adhikari, S. Current Status of Hydrogen Production Techniques by Steam Reforming of Ethanol: A Review. *Energy Fuels* **2005**, *19* (5), 2098–2106.
- (3) Shobeyrian, F.; Shojaei, F.; Soleimani, M.; Pourfath, M. Two-Dimensional Cr<sub>2</sub>X<sub>2</sub>Y<sub>6</sub> (X = Si, Ge; Y = S, Se, Te) Family with Potential Application in Photocatalysis. *Appl. Surf. Sci.* **2023**, *630* (May), 157319.
- (4) Ehrlich, S.; Moellmann, J.; Reckien, W.; Bredow, T.; Grimme, S. System-Dependent Dispersion Coefficients for the DFT-D3 Treatment of Adsorption Processes on Ionic Surfaces. *ChemPhysChem* **2011**, *12* (17), 3414–3420.
- (5) Singh, A. K.; Mathew, K.; Zhuang, H. L.; Hennig, R. G. Computational Screening of 2D Materials for Photocatalysis. *J. Phys. Chem. Lett.* **2015**, *6* (6), 1087–1098.
- (6) Szilágyi, I. M.; Fórizs, B.; Rosseler, O.; Szegedi, A.; Németh, P.; Király, P.; Tárkányi, G.; Vajna, B.; Varga-Josepovits, K.; László, K.; Tóth, A. L.; Baranyai, P.; Leskelä, M. WO<sub>3</sub> Photocatalysts: Influence of Structure and Composition. *J. Catal.* **2012**, *294* (October), 119–127.
- (7) Cheng, L.; Xiang, Q.; Liao, Y.; Zhang, H. CdS-Based Photocatalysts. *Energy Environ. Sci.* **2018**, *11* (6), 1362–1391.
- (8) Lee, G. J.; Wu, J. J. Recent Developments in ZnS Photocatalysts from Synthesis to Photocatalytic Applications — A Review. *Powder Technol.* **2017**, *318*, 8–22.
- (9) Di Liberto, G.; Tosoni, S.; Pacchioni, G. Role of Surface Termination in Forming Type-II Photocatalyst Heterojunctions: The Case of TiO<sub>2</sub>/BiVO<sub>4</sub>. *J. Phys.: Condens. Matter* **2020**, *33* (7), 075001.
- (10) Cerrato, E.; Gionco, C.; Paganini, M. C.; Giamello, E.; Albanese, E.; Pacchioni, G. Origin of Visible Light Photoactivity of the CeO<sub>2</sub>/ZnO Heterojunction. *ACS Appl. Energy Mater.* **2018**, *1* (8), 4247–4260.
- (11) Eshete, M.; Li, X.; Yang, L.; Wang, X.; Zhang, J.; Xie, L.; Deng, L.; Zhang, G.; Jiang, J. Charge Steering in Heterojunction Photocatalysis: General Principles, Design, Construction, and Challenges. *Small Sci.* **2023**, *3* (3), 2200041.
- (12) Zhao, Y.; Zhang, S.; Shi, R.; Waterhouse, G. I. N.; Tang, J.; Zhang, T. Two-Dimensional Photocatalyst Design: A Critical Review

of Recent Experimental and Computational Advances. *Mater. Today* **2020**, *34* (xx), 78–91.

(13) Oh, S. M.; Patil, S. B.; Jin, X.; Hwang, S. J. Recent Applications of 2D Inorganic Nanosheets for Emerging Energy Storage System. *Chem.—A Eur. J.* **2018**, *24* (19), 4757–4773.

(14) Tao, H.; Gao, Y.; Talreja, N.; Guo, F.; Texter, J.; Yan, C.; Sun, Z. Two-Dimensional Nanosheets for Electrocatalysis in Energy Generation and Conversion. *J. Mater. Chem. A* **2017**, *5* (16), 7257–7284.

(15) Dai, W.; Ren, K.; Zhu, Y.; Pan, Y.; Yu, J.; Lu, T. Flower-like  $\text{CoNi}_2\text{S}_4/\text{Ni}_3\text{S}_2$  Nanosheet Clusters on Nickel Foam as Bifunctional Electrocatalyst for Overall Water Splitting. *J. Alloys Compd.* **2020**, *844*, 156252.

(16) Nicks, J.; Sasitharan, K.; Prasad, R. R. R.; Ashworth, D. J.; Foster, J. A. Metal–Organic Framework Nanosheets: Programmable 2D Materials for Catalysis, Sensing, Electronics, and Separation Applications. *Adv. Funct. Mater.* **2021**, *31* (42), 2103723.

(17) Gan, J.; Lu, X.; Tong, Y. Towards Highly Efficient Photoanodes: Boosting Sunlight-Driven Semiconductor Nanomaterials for Water Oxidation. *Nanoscale* **2014**, *6* (13), 7142–7164.

(18) Su, T.; Shao, Q.; Qin, Z.; Guo, Z.; Wu, Z. Role of Interfaces in Two-Dimensional Photocatalyst for Water Splitting. *ACS Catal.* **2018**, *8* (3), 2253–2276.

(19) Liu, X.; Cheng, P.; Zhang, X.; Shen, T.; Liu, J.; Ren, J. C.; Wang, H.; Li, S.; Liu, W. Enhanced Solar-to-Hydrogen Efficiency for Photocatalytic Water Splitting Based on a Polarized Heterostructure: The Role of Intrinsic Dipoles in Heterostructures. *J. Mater. Chem. A* **2021**, *9* (25), 14515–14523.

(20) Ren, K.; Wang, K.; Cheng, Y.; Tang, W.; Zhang, G. Two-Dimensional Heterostructures for Photocatalytic Water Splitting: A Review of Recent Progress. *Nano Futures* **2020**, *4* (3), 032006.

(21) Idrees, M.; Amin, B.; Chen, Y.; Yan, X. Computation Insights of  $\text{MoS}_2\text{-CrXY}$  ( $X \neq Y$  S, Se, Te) van Der Waals Heterostructure for Spintronic and Photocatalytic Water Splitting Applications. *Int. J. Hydrogen Energy* **2024**, *51*, 1217–1228.

(22) Wang, J.; Xuan, J.; Wei, X.; Zhang, Y.; Fan, J.; Ni, L.; Yang, Y.; Liu, J.; Tian, Y.; Duan, L. Direct Z-Scheme  $\text{GaTe}/\text{SnS}_2$  van Der Waals Heterojunction with Tunable Electronic Properties: A Promising Highly Efficient Photocatalyst. *Int. J. Hydrogen Energy* **2024**, *54* (September 2023), 979–989.

(23) Mao, Y.; Xu, C.; Yuan, J.; Zhao, H. A Two-Dimensional  $\text{GeSe}/\text{SnSe}$  Heterostructure for High Performance Thin-Film Solar Cells. *J. Mater. Chem. A* **2019**, *7* (18), 11265–11271.

(24) Wang, G.; Xie, W.; Guo, S.; Chang, J.; Chen, Y.; Long, X.; Zhou, L.; Ang, Y. S.; Yuan, H. Two-Dimensional  $\text{GeC}/\text{MX}_2$  ( $M = \text{Zr}, \text{Hf}$ ;  $X, Y = \text{S}, \text{Se}$ ) Heterojunctions Used as Highly Efficient Overall Water-Splitting Photocatalysts. *Molecules* **2024**, *29* (12), 2793.

(25) Zhou, H.; Cai, W.; Li, J.; Liu, X.; Xiong, W.; Zhou, Y.; Xu, Z.; Wang, B.; Ye, C.  $\text{C}_2\text{N}/\text{BlueP}$  van Der Waals Hetero-Structure: An Efficient Photocatalytic Water Splitting 2D Material. *Phys. Chem. Chem. Phys.* **2020**, *22* (3), 1485–1492.

(26) Wang, Q.; Zhu, Q.; Cao, L.; Fan, L.; Gu, F.; Zhang, Y.; Zheng, C.; Xiong, S.; Xu, L. Two-Dimensional  $\text{SiH}/\text{g-C}_3\text{N}_4$  van Der Waals Type-II Heterojunction Photocatalyst: A New Effective and Promising Photocatalytic Material. *Coatings* **2024**, *14* (3), 263.

(27) Ren, K.; Yu, J.; Tang, W. Two-Dimensional  $\text{ZnO}/\text{BSe}$  van Der Waals Heterostructure Used as a Promising Photocatalyst for Water Splitting: A DFT Study. *J. Alloys Compd.* **2020**, *812*, 152049.

(28) Wang, B. J.; Li, X. H.; Zhao, R.; Cai, X. L.; Yu, W. Y.; Li, W. B.; Liu, Z. S.; Zhang, L. W.; Ke, S. H. Electronic Structures and Enhanced Photocatalytic Properties of Blue Phosphorene/BSe van Der Waals Heterostructures. *J. Mater. Chem. A* **2018**, *6* (19), 8923–8929.

(29) Liang, Y.; Long, C.; Li, J.; Jin, H.; Huang, B.; Dai, Y. InSe Monolayer: Promising Cocatalyst of  $\text{g-C}_3\text{N}_4$  for Water Splitting under Visible Light. *ACS Appl. Energy Mater.* **2018**, *1* (10), 5394–5401.

(30) Zhu, M.; Sun, Z.; Fujitsuka, M.; Majima, T. Z-Scheme Photocatalytic Water Splitting on a 2D Heterostructure of Black Phosphorus/Bismuth Vanadate Using Visible Light. *Angew. Chem., Int. Ed.* **2018**, *57* (8), 2160–2164.

(31) Liang, Y.; Li, J.; Jin, H.; Huang, B.; Dai, Y. Photoexcitation Dynamics in Janus- $\text{MoSSe}/\text{WSe}_2$  Heterobilayers: Ab Initio Time-Domain Study. *J. Phys. Chem. Lett.* **2018**, *9* (11), 2797–2802.

(32) Ashwin Kishore, M. R.; Larsson, K.; Ravindran, P. Two-Dimensional  $\text{CdX}/\text{C}_2\text{N}$  ( $X = \text{S}, \text{Se}$ ) Heterostructures as Potential Photocatalysts for Water Splitting: A DFT Study. *ACS Omega* **2020**, *5* (37), 23762–23768.

(33) Zhang, Z.; Qian, Q.; Li, B.; Chen, K. J. Interface Engineering of Monolayer  $\text{MoS}_2/\text{GaN}$  Hybrid Heterostructure: Modified Band Alignment for Photocatalytic Water Splitting Application by Nitridation Treatment. *ACS Appl. Mater. Interfaces* **2018**, *10* (20), 17419–17426.

(34) Chen, X.; Han, W.; Tian, Z.; Yue, Q.; Peng, C.; Wang, C.; Wang, B.; Yin, H.; Gu, Q. Exploration of Photocatalytic Overall Water Splitting Mechanisms in the Z-Scheme  $\text{SnS}_2/\beta\text{-As}$  Heterostructure. *J. Phys. Chem. C* **2023**, *127* (13), 6347–6355.

(35) Ghosh, A.; Pramanik, A.; Pal, S.; Sarkar, P. Emergence of Z-Scheme Photocatalysis for Total Water Splitting: An Improvised Route to High Efficiency. *J. Phys. Chem. Lett.* **2024**, *15* (26), 6841–6851.

(36) Sa, B.; Hu, R.; Zheng, Z.; Xiong, R.; Zhang, Y.; Wen, C.; Zhou, J.; Sun, Z. High-Throughput Computational Screening and Machine Learning Modeling of Janus 2D III–VI van Der Waals Heterostructures for Solar Energy Applications. *Chem. Mater.* **2022**, *34* (15), 6687–6701.

(37) Kresse, G.; Hafner, J. Ab Initio Molecular Dynamics for Liquid Metals. *Phys. Rev. B* **1993**, *47* (1), 558.

(38) Heyd, J.; Scuseria, G. E.; Ernzerhof, M. Hybrid Functionals Based on a Screened Coulomb Potential. *J. Chem. Phys.* **2003**, *118* (18), 8207–8215.

(39) Grimme, S.; Antony, J.; Ehrlich, S.; Krieg, H. A Consistent and Accurate Ab Initio Parametrization of Density Functional Dispersion Correction (DFT-D) for the 94 Elements H–Pu. *J. Chem. Phys.* **2010**, *132*, 154104.

(40) Bersuker, I. B. Dipole Moments of Symmetrical Molecular Systems. *Theor. Exp. Chem.* **1969**, *5* (3), 188–191.

(41) Sander, T.; Maggio, E.; Kresse, G. Beyond the Tamm–Dancoff Approximation for Extended Systems Using Exact Diagonalization. *Phys. Rev. B: Condens. Matter Mater. Phys.* **2015**, *92* (4), 1–14.

(42) Gjerding, M. N.; Taghizadeh, A.; Rasmussen, A.; Ali, S.; Bertoldo, F.; Deilmann, T.; Knøsgaard, N. R.; Kruse, M.; Larsen, A. H.; Manti, S.; et al. Recent Progress of the Computational 2D Materials Database (C2DB). *2D Mater.* **2021**, *8* (4), 044002.

(43) Flores, M. Z. S.; Autreto, P. A. S.; Legoas, S. B.; Galvao, D. S. Graphene to Graphane: A Theoretical Study. *Nanotechnology* **2009**, *20* (46), 465704.

(44) Sun, M.; Chou, J.-P.; Zhao, Y.; Yu, J.; Tang, W. Weak CH Center Dot Center Dot Center Dot FC Hydrogen Bonds Make a Big Difference in Graphane/Fluorographane and Fluorographane/Fluorographane Bilayers. *Phys. Chem. Chem. Phys.* **2017**, *19* (41), 28127–28132.

(45) Fang, D. Q.; Zhang, Y.; Zhang, S. L. Silicane Nanoribbons: Electronic Structure and Electric Field Modulation. *New J. Phys.* **2014**, *16* (11), 115006.

(46) Niu, M.; Cheng, D.; Cao, D.  $\text{SiH}/\text{TiO}_2$  and  $\text{GeH}/\text{TiO}_2$  Heterojunctions: Promising  $\text{TiO}_2$ -Based Photocatalysts under Visible Light. *Sci. Rep.* **2014**, *4* (1), 4810.

(47) Hu, L.; Zhao, J.; Yang, J. First Principles Study of Fluorine Substitution on Two-Dimensional Germanane. *J. Phys.: Condens. Matter* **2014**, *26* (33), 335302.

(48) Şahin, H.; Cahangirov, S.; Topsakal, M.; Bekaroglu, E.; Akturk, E.; Senger, R. T.; Ciraci, S. Monolayer Honeycomb Structures of Group-IV Elements and III–V Binary Compounds: First-Principles Calculations. *Phys. Rev. B: Condens. Matter Mater. Phys.* **2009**, *80* (15), 155453.

(49) Yin, H.; Gao, J.; Zheng, G.-P.; Wang, Y.; Ma, Y. Giant Piezoelectric Effects in Monolayer Group-V Binary Compounds with Honeycomb Phases: A First-Principles Prediction. *J. Phys. Chem. C* **2017**, *121* (45), 25576–25584.

(50) Kaur, S.; Kumar, A.; Srivastava, S.; Tankeshwar, K. Electronic Structure Engineering of Various Structural Phases of Phosphorene. *Phys. Chem. Chem. Phys.* **2016**, *18* (27), 18312–18322.

(51) Yu, W.; Niu, C.-Y.; Zhu, Z.; Wang, X.; Zhang, W.-B. Atomically Thin Binary V–V Compound Semiconductor: A First-Principles Study. *J. Mater. Chem. C* **2016**, *4* (27), 6581–6587.

(52) Rahman, A.; Kim, H. J.; Noor-A-Alam, M.; Shin, Y.-H. A Theoretical Study on Tuning Band Gaps of Monolayer and Bilayer SnS<sub>2</sub> and SnSe<sub>2</sub> under External Stimuli. *Curr. Appl. Phys.* **2019**, *19* (6), 709–714.

(53) Gomes, L. C.; Carvalho, A.; Castro Neto, A. H. Vacancies and Oxidation of Two-Dimensional Group-IV Monochalcogenides. *Phys. Rev. B* **2016**, *94* (5), 54103.

(54) Ding, Y.; Wang, Y.; Ni, J.; Shi, L.; Shi, S.; Tang, W. First Principles Study of Structural, Vibrational and Electronic Properties of Graphene-like MX<sub>2</sub> (M= Mo, Nb, W, Ta; X= S, Se, Te) Monolayers. *Phys. B* **2011**, *406* (11), 2254–2260.

(55) Chen, J.; Tan, X.; Lin, P.; Sa, B.; Zhou, J.; Zhang, Y.; Wen, C.; Sun, Z. Comprehensive Understanding of Intrinsic Mobility in the Monolayers of III–VI Group 2D Materials. *Phys. Chem. Chem. Phys.* **2019**, *21* (39), 21898–21907.

(56) Jiang, H. R.; Shyy, W.; Liu, M.; Wei, L.; Wu, M. C.; Zhao, T. S. Boron Phosphide Monolayer as a Potential Anode Material for Alkali Metal-Based Batteries. *J. Mater. Chem. A* **2017**, *5* (2), 672–679.

(57) Mortazavi, B.; Shojaei, F.; Rabczuk, T.; Zhuang, X. High Tensile Strength and Thermal Conductivity in BeO Monolayer: A First-Principles Study. *FlatChem* **2021**, *28*, 100257.

(58) Wang, Z.; Zhu, W. Tunable Band Alignments in 2D Ferroelectric  $\alpha$ -In<sub>2</sub>Se<sub>3</sub>Based Van Der Waals Heterostructures. *ACS Appl. Electron. Mater.* **2021**, *3* (11), 5114–5123.

(59) Lee, C. H.; Lee, G. H.; Van Der Zande, A. M.; Chen, W.; Li, Y.; Han, M.; Cui, X.; Arefe, G.; Nuckolls, C.; Heinz, T. F.; Guo, J.; Hone, J.; Kim, P. Atomically Thin P-n Junctions with van Der Waals Heterointerfaces. *Nat. Nanotechnol.* **2014**, *9* (9), 676–681.

(60) Rivera, P.; Schaibley, J. R.; Jones, A. M.; Ross, J. S.; Wu, S.; Aivazian, G.; Klement, P.; Seyler, K.; Clark, G.; Ghimire, N. J.; Yan, J.; Mandrus, D. G.; Yao, W.; Xu, X. Observation of Long-Lived Interlayer Excitons in Monolayer MoSe<sub>2</sub>-WSe<sub>2</sub> Heterostructures. *Nat. Commun.* **2015**, *6*, 4–9.

(61) Lazić, P. CellMatch: Combining Two Unit Cells into a Common Supercell with Minimal Strain. *Comput. Phys. Commun.* **2015**, *197*, 324–334.

(62) Pandey, T.; Parker, D. S.; Lindsay, L. Ab Initio Phonon Thermal Transport in Monolayer InSe, GaSe, GaS, and Alloys. *Nanotechnology* **2017**, *28* (45), 455706.

(63) Mortazavi, B. Ultrahigh Thermal Conductivity and Strength in Direct-Gap Semiconducting Graphene-like BC<sub>6</sub>N: A First-Principles and Classical Investigation. *Carbon* **2021**, *182*, 373–383.

(64) Pakdel, S.; Rasmussen, A.; Taghizadeh, A.; Kruse, M.; Olsen, T.; Thygesen, K. S. High-Throughput Computational Stacking Reveals Emergent Properties in Natural van Der Waals Bilayers. *Nat. Commun.* **2024**, *15* (1), 932.

(65) Shahrokhi, M.; Le Bahers, T.; Raybaud, P. Tailoring the Optoelectronic Properties and Dielectric Profiles of Few-Layer S-Doped MoO<sub>3</sub> and O-Doped MoS<sub>2</sub> Nanosheets: A First-Principles Study. *Phys. Chem. Chem. Phys.* **2022**, *24* (41), 25440–25451.

(66) Palanivel, B.; Mani, A. Conversion of a Type-II to a Z-Scheme Heterojunction by Intercalation of a 0D Electron Mediator between the Integrative NiFe<sub>2</sub>O<sub>4</sub>/g-C<sub>3</sub>N<sub>4</sub> Composite Nanoparticles: Boosting the Radical Production for Photo-Fenton Degradation. *ACS Omega* **2020**, *5* (31), 19747–19759.

(67) Lv, T.; Li, J.; Arif, N.; Qi, L.; Lu, J.; Ye, Z.; Zeng, Y. J. Polarization and External-Field Enhanced Photocatalysis. *Matter* **2022**, *5* (9), 2685–2721.

(68) Tang, W.; Sanville, E.; Henkelman, G. A Grid-Based Bader Analysis Algorithm without Lattice Bias. *J. Phys.: Condens. Matter* **2009**, *21* (8), 084204.

(69) Meng, J.; Wang, J.; Wang, J.; Li, Q.; Yang, J.  $\beta$ -SnS/GaSe Heterostructure: A Promising Solar-Driven Photocatalyst with Low

Carrier Recombination for Overall Water Splitting. *J. Mater. Chem. A* **2022**, *10* (7), 3443–3453.

(70) Shahrokhi, M.; Raybaud, P.; Le Bahers, T. 2D MoO<sub>3</sub>-XS<sub>x</sub>/MoS<sub>2</sub> van Der Waals Assembly: A Tunable Heterojunction with Attractive Properties for Photocatalysis. *ACS Appl. Mater. Interfaces* **2021**, *13* (30), 36465–36474.



CAS BIOFINDER DISCOVERY PLATFORM™

**ELIMINATE DATA SILOS. FIND WHAT YOU NEED, WHEN YOU NEED IT.**

A single platform for relevant, high-quality biological and toxicology research

**Streamline your R&D**

CAS  
A Division of the American Chemical Society